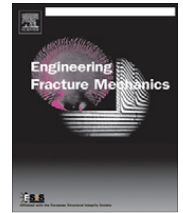




Contents lists available at ScienceDirect

Engineering Fracture Mechanics

journal homepage: www.elsevier.com/locate/engfracmech

Non-local modeling of thermal shock damage in refractory materials

F. Damhof^{a,*}, W.A.M. Brekelmans^b, M.G.D. Geers^b^a Corus Research Development and Technology, P.O. Box 10000, 1970CA IJmuiden, The Netherlands^b Faculty of Mechanical Engineering, Eindhoven University of Technology, P.O. Box 513, 5600MB Eindhoven, The Netherlands

ARTICLE INFO

Article history:

Received 12 July 2007

Received in revised form 14 March 2008

Accepted 4 June 2008

Available online 9 July 2008

Keywords:

Damage mechanics

Ceramics

Failure assessment

Structural assessment

Higher order continuum

ABSTRACT

A non-local damage framework has been coupled with heat transport to model transient thermo-mechanical damage (in particular thermal shock) in refractory materials. The non-locality, to be dealt with to obtain an adequate problem formulation, is introduced by terms accounting for micro-structural strain gradients induced by transient temperature gradients. The parameters figuring in the evolution law for elasticity-based damage are temperature dependent. Damage due to isotropic thermal expansion has been accounted for by proposing a new evolution law. A single variable for the total damage is obtained by combining both damage mechanisms. The influence of non-locality and transient temperature gradients within non-locality is investigated in numerical examples. The phenomenological relevance of the framework is verified by modeling of experiments, which simulate thermal shock under process conditions.

© 2008 Elsevier Ltd. All rights reserved.

1. Introduction

Refractory materials are used in linings of installations for iron and steel making with operating temperatures as high as 1800 °C. Major cause leading to early failure of such installations is the wear of the refractory material due to fatal thermal stresses. This happens, e.g., when molten metal is introduced into a relatively cold ladle. Another example is the sudden opening of an operating furnace where hot refractory material suddenly becomes exposed to cold air leading again to severe thermal stresses. The generation of such stresses is generally referred to as thermal shock.

In the past, various approaches have been used to model thermal shock in refractory materials. Parameters describing the effect of thermal shock in refractory materials were defined by Hasselman [1–3] and Lu and Fleck [4]. Also numerous analytical efforts have been undertaken to model thermal shock cracks in ceramic materials [5–11]. The application of the finite element method permitted the study of evolution of thermal stresses and cracks by modeling parts of or even complete installations forming input to an improved re-design [12–18]. Despite the quasi-brittle character of refractory materials early computer modeling was mostly based on linear elastic fracture mechanics. At a later stage quasi-brittleness was incorporated using fictitious crack models with fit-for-purpose constitutive laws [19,20] extended with gradient terms to model size effects correctly [21]. Latest efforts entail consideration of the complex micro-structure of refractory material [22] and multi-scale models covering sizes from granular level up to full-size installations [23].

At thermal shock sensitive locations in installations coarse-grained refractory material is applied with grain sizes up to 5 mm. Such refractories show a diffuse (micro-)crack pattern upon exposure to thermal shock. Simonin et al. [24] report for a coarse-grained high-alumina refractory material both diffuse and localized thermal shock damage. Mismatch in thermal expansion of grains and matrix causes micro-cracks leading to diffuse thermal shock damage [25,26] catalyzed by pre-existing micro-cracks stemming from the refractory production process. Boussuge [27,28] confirmed that coarse-grained

* Corresponding author. Tel.: +31 251 498049; fax: +31 251 470489.
E-mail address: erik.damhof@corusgroup.com (F. Damhof).

Nomenclature

σ	stress tensor
ε	strain tensor
ε_{th}	thermal strain tensor
ε_{el}	elastic strain tensor
θ	temperature
θ_0	reference temperature
α_{th}	coefficient of thermal expansion
D	damage variable
4C	elasticity tensor
ν	Poisson's ratio
E	Young's modulus
E_0	Young's modulus at reference state
V	sound velocity
η	tension–compression sensitivity
ε_{eq}	local equivalent strain
$\bar{\varepsilon}_{eq}$	non-local equivalent strain
$\varepsilon_{eq,micro}$	micro-structural equivalent strain
l_c	internal length scale
r_{ths}	proportionality constant
c_{ths}	proportionality constant
κ_{el}	history variable for elastic damage
$\kappa_{el,i}$	initiation history parameter for elastic damage
α	first evolution parameter for elastic damage
β	second evolution parameter for elastic damage
κ_{th}	history variable for thermal damage
$\kappa_{th,i}$	initiation history parameter for thermal damage
$\kappa_{th,c}$	first evolution parameter for thermal damage
ϕ	first evolution parameter for elastic damage
α_{dif}	coefficient of thermal diffusion
λ	thermal conductivity
ρ	density
C_p	thermal capacity
$\underline{N}_j, j = \theta, u, e$	interpolation functions for respectively: temperature, displacement, non-local equivalent strain
$\underline{B}_j, j = \theta, u, e$	gradient matrix for respectively: temperature, displacement, non-local equivalent strain
σ	column with components of stress tensor
\tilde{a}	column with nodal degrees of freedom
$\tilde{\theta}$	column with nodal temperatures
\tilde{u}	column with nodal displacements
$\tilde{\varepsilon}$	column with nodal non-local equivalent strains
\tilde{K}_{i-1}^{eq}	system matrix at iteration $i - 1$
θ	index for temperature
u	index for displacement
e	index for non-local equivalent strain
$K_{i-1}^{v,w}, v, w = \theta, u, e$	sub-matrix of system matrix at iteration $i - 1$
$f_{ext}^v, v = \theta, u, e$	column with respectively external nodal heat fluxes, mechanical forces and zero elements
$f_{int,i-1}^v, v = \theta, u, e$	column with internal nodal reactions for respectively temperature, displacement, non-local equivalent strain at iteration $i - 1$

refractories develop a distributed damage preceding localization and proposes continuum damage mechanics [29] to model the material behaviour.

In the past various authors reported on modeling the thermo-mechanical behaviour of refractory materials based on damage mechanics. Headrick et al. [30] model combined thermo-mechanical and chemical damage in an alumina-silicate refractory lining of a gasifier. Separate damage variables are used for compressive and tensile failure. Prompt et al. [31] analyse the wear of a blast furnace duct. Based on the observed fracture pattern of micro- and macro-cracks due to high transient thermal gradients a continuum damage approach was adopted. A single damage variable was satisfactorily used to describe damage originating from a compressive stress state at the hot face and from a tensile stress state inside the refractory lining. Liang and Headrick [32] model filling of an alumina refractory cup using separate damage variables for compressive and tensile damage. The total damage is found via a multiplicative combination of the damage variables.

More advanced models are employed predicting damage in concrete exposed to elevated temperatures in a fire. Elasticity-based damage is combined with thermal damage (e.g. from micro-cracking due to isotropic thermal expansion). Total damage is obtained via a multiplicative combination of both damage descriptions. Gawin et al. [35] follow a scalar damage approach while the constitutive behaviour is distinct for compression and tension. Damage evolution parameters are assumed temperature independent. Luccioni et al. [34] perform a similar exercise where thermal damage manifests itself through the deterioration of Young's modulus including an effect on Poisson's ratio. Nentech et al. [33] use separate compressive and tensile damage variables combined with hardening plasticity. A third damage variable is used to account for thermal damage. It was proposed to incorporate an internal length scale (representing the dimensions of the material micro-structure) into the constitutive equations to preserve the well-posedness of the problem upon strain localization and to avoid mesh dependency in a finite element analysis. This can be realized by using, e.g., a non-local equivalent strain measure as was shown by Stabler and Baker [36,37] who model damage due to temperature gradients (elasticity-based damage) combined with thermal damage. The elasticity-based damage is activated by a non-local strain measure obtained via Gaussian weighting applied to the local equivalent strain field. Pearce et al. [38] also follow a non-local approach incorporating elasticity-based and thermal damage with temperature-dependent evolution parameters. The non-local strain measure is, however, obtained via an implicit gradient enhanced formulation as advocated by Peerlings et al. [39,40] to preserve mathematical well-posedness. None of the approaches mentioned in this paragraph reflect on fine scale thermal shock damage originating from thermal expansion mismatches in the micro-structural constituents. Furthermore, the transient evolution of non-local damage was not investigated and the incorporation of temperature dependency in the damage frameworks was found incomplete as to correctly describe the temperature-dependent mechanical behaviour of refractory material.

To represent transient temperature damage in granular coarse-grained refractory material it is proposed in this paper to model elasticity-based (thermal shock) damage isotropically. This is combined with a newly described evolution of thermal damage in an additive manner implying that both damage mechanisms act independently. This is justified by the fact that the elastic damage predominantly works macroscopically, whereas the origin of thermal damage is of microscopic nature. The total damage thus represents a separation of macroscopic and microscopic scales. The driving variable for elasticity-based damage, the non-local equivalent strain, is obtained via a gradient enhanced implicit formulation. Coupling of this formulation with elastic equilibrium and transient heat transport leads to transient non-local damage evolution which has not been modeled before. Contrary to previous works on disintegration of concrete and refractories at elevated temperature, the elasticity-based damage evolution law uses temperature-dependent parameters. The modified Von Mises definition in [39], used to obtain the local equivalent strain, is enhanced in this paper by the incorporation of a temperature-dependent ratio of compressive and tensile strength. The existing non-locality equation is in this paper extended with a term accounting for fine scale transient thermal shock damage. A full Newton–Raphson scheme is used to implement the presented field equations in a Galerkin based finite element framework. In sensitivity analyses the influence of the contribution of said fine scale thermal shock damage as well as an increasing internal length scale is investigated. The phenomenological relevance of the modeling framework is established by comparing the data from thermal shock experiments with the numerical model thereof.

2. Temperature-dependent mechanical behaviour

The areas within high temperature installations prone to thermal shock are equipped with specifically tailored refractory materials. A typical example of the chemical composition of such a refractory material is presented in Fig. 1 (left). The weight percentages of alumina (Al_2O_3) and silica (SiO_2) govern to a large extent the thermo-mechanical characteristics of the material. Generally, a larger alumina content leads to a lower thermal shock resistance. Nonetheless alumina-silicate bricks are used in harsh high temperature environments because of their high temperature strength combined with a reasonable thermal shock resistance. Such bricks are mainly composed of mullite ($3\text{Al}_2\text{O}_3 \cdot 2\text{SiO}_2$) with some glassy phases of SiO_2 , generally

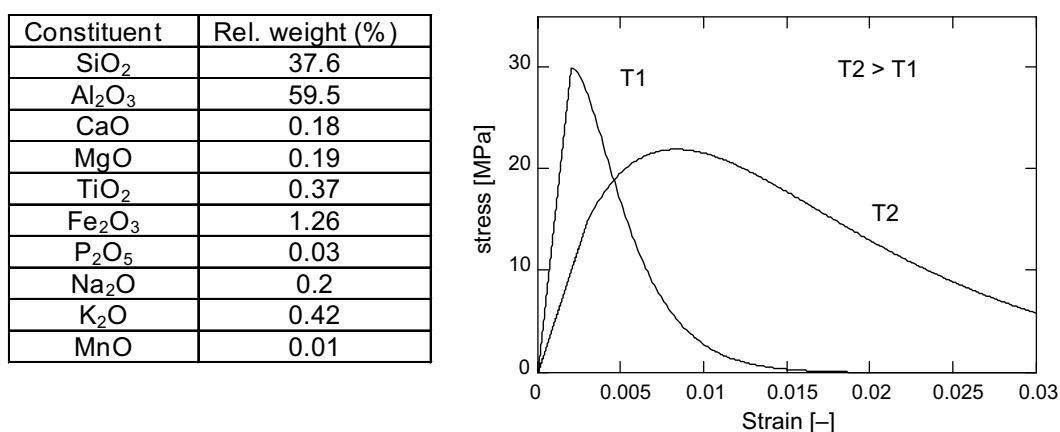


Fig. 1. Chemical composition (left) and temperature-dependent mechanical response of a typical alumina-silicate brick (right).

located around the grain boundaries. These glassy phases begin to soften when approaching their glass transition temperature leading to a quasi-brittle behaviour at higher temperatures [41]. Usually, this glass transition temperature lies well below the ultimate usage temperature of the refractory material. Fig. 1 (right) shows a typical uni-axial response in tension of a dense refractory material. Upon temperature increase a transition from purely brittle towards a more quasi-brittle behaviour takes place; the post-elastic tail preceding ultimate failure becomes longer. Also the strain at which the peak stress occurs, increases with temperature. Other characteristic changes at increasing temperature are a lower strength and a lower Young's modulus. The aforementioned temperature dependencies need to be incorporated into the constitutive model.

3. Constitutive model

3.1. Damage evolution

The total strain in a thermo-mechanically loaded refractory material is composed of a thermal strain and an elastic strain defined with respect to a predefined reference configuration. The thermal strain is due to the isotropic thermal expansion following a temperature increase with respect to the reference. The elastic strain originates from stresses due to external material constraints (e.g. neighboring bricks) and due to the constrained thermal expansion within the material itself. The total strain tensor is decomposed according to:

$$\varepsilon = \varepsilon_{th} + \varepsilon_{el} \quad (1)$$

where ε_{th} and ε_{el} represent the thermal and elastic strain tensor, respectively. The thermal strain tensor can be written as

$$\varepsilon_{th} = \alpha_{th}(\theta - \theta_0)\mathbf{I} \quad (2)$$

where α_{th} is the thermal expansion coefficient, θ and θ_0 denote the actual temperature and the reference temperature in the unstrained state, respectively, and \mathbf{I} is the identity tensor. For isotropic elastic damage affected behaviour, Hooke's law reads

$$\sigma = (1 - D)^4 \mathbf{C} : (\varepsilon - \varepsilon_{th}) \quad (3)$$

where the damage D accounts for both the elasticity-based and the thermal damage. The fourth-order tensor ${}^4\mathbf{C}$ contains the temperature-dependent elasticity moduli of the undamaged material. The elasticity-based damage is predominantly a macroscopic phenomenon, whereas thermal damage is of microscopic origin and induced by thermal expansion mismatches within the micro-structure of the material. For lower damage levels this implies a separation of macroscopic (elastic damage) and microcopic (thermal damage) scales and independently acting damage mechanisms. Hence the total damage D can be written as

$$0 \leq D = d_{el} + d_{th} \leq 1 \quad (4)$$

where d_{el} represents the elasticity-based damage and d_{th} the thermal damage.

For the elasticity-based damage the following evolution law is proposed [39]:

$$d_{el} = 1 - \frac{\kappa_{el,i}}{\kappa_{el}} [(1 - \alpha) + \alpha e^{-\beta(\kappa_{el} - \kappa_{el,i})}] \quad (5)$$

where κ_{el} is the damage driving variable, $\kappa_{el,i}$ denotes its minimum threshold value, α and β are temperature-dependent material parameters where the latter reflects the brittleness of the material. The driving variable κ_{el} is determined through the Kuhn-Tucker relations for damage evolution:

$$\dot{\kappa}_{el} \geq 0, \quad \bar{\varepsilon}_{eq} - \kappa_{el} \leq 0, \quad \dot{\kappa}_{el}(\bar{\varepsilon}_{eq} - \kappa_{el}) = 0 \quad (6)$$

where $\bar{\varepsilon}_{eq}$ represents the non-local equivalent strain which equals κ_{el} upon damage evolution. The local and non-local equivalent strains are defined in detail in Section 3.2. The temperature-dependency of the material parameters α and β may cause an unphysical decrease of the damage unless the numerical implementation is adequately adapted to prevent this inconsistency.

The driving variable for the thermal damage is the maximum attained temperature within the material. A uniform temperature increase induces an isotropic thermal expansion. When the temperature exceeds a certain threshold value small (microscopic) cracks might appear causing irreversible thermal damage [33–38]. From a structural point of view this thermal damage is a typical fine scale micro-structural mechanism, associated to local mismatches in elastic and thermal properties of the constituent phases in the micro-structure. On the other hand certain chemical components of refractory material (e.g. SiO₂) might be subject to phase changes at elevated temperatures. This can lead to a change in the material structure (e.g. local volume changes) and a permanently decreased Young's modulus, which thus also contributes to the thermal damage. For the evolution of thermal damage a new evolution law is proposed:

$$d_{th} = 1 + \sin \left(\frac{1}{2} \pi \left(3 - \left(\frac{\kappa_{th} - \kappa_{th,i}}{\kappa_{th,c} - \kappa_{th,i}} \right)^\phi \right) \right) \quad (7)$$

where κ_{th} represents the driving variable for thermal damage: the attained maximum temperature. The parameters $\kappa_{th,i}$ and $\kappa_{th,c}$ denote, respectively, the initial and critical temperature for thermal damage. When κ_{th} approaches $\kappa_{th,c}$ the thermal damage would become 1. Normally, process temperatures will never reach $\kappa_{th,c}$ and consequently thermal damage will never reach the value 1. The parameter ϕ in Eq. (7) can be chosen such that the thermal damage increases progressively, linear or degressively at increase of the maximum attained temperature. The driving variable κ_{th} is subject to the Kuhn–Tucker relations for the thermal damage evolution:

$$\dot{\kappa}_{th} \geq 0, \quad \theta - \kappa_{th} \leq 0, \quad \dot{\kappa}_{th}(\theta - \kappa_{th}) = 0 \quad (8)$$

3.2. Equivalent strain

For the local equivalent strain the modified Von Mises definition [39] is suitable:

$$\varepsilon_{eq} = \frac{\eta - 1}{2\eta(1 - 2\nu)} J_1 + \frac{1}{2\eta} \sqrt{\left(\frac{\eta - 1}{1 - 2\nu}\right)^2 J_1^2 + \frac{6\eta}{(1 + \nu)^2} J_2} \quad (9)$$

where η is the temperature-dependent ratio of compressive and tensile strength such that an uni-axial compressive stress $\eta\sigma$ leads to identical damage as a tensile stress equal to σ ; J_1 and J_2 are invariants of the elastic strain tensor ε_{el} :

$$J_1 = \text{tr}(\varepsilon_{el}), \quad J_2 = \text{tr}(\varepsilon_{el} \cdot \varepsilon_{el}) - \frac{1}{3} \text{tr}^2(\varepsilon_{el}) \quad (10)$$

The formulation of κ_{el} according to (6) in terms of a local equivalent strain as described in Eq. (9) would lead to a pathological mesh dependency in finite element solutions [39]. This can be resolved by adopting a non-local approach involving a weighted average of the equivalent strains within a certain vicinity of a material point. This can, e.g., be achieved by using an integral format:

$$\bar{\varepsilon}_{eq}(\vec{x}) = \int_V g(\vec{\xi}) \varepsilon_{eq}(\vec{x} + \vec{\xi}) dV \quad (11)$$

where the non-local equivalent strain $\bar{\varepsilon}_{eq}(\vec{x})$ is the weighted volume average of the local equivalent strain ε_{eq} . Furthermore, $g(\vec{\xi})$ is a weight function and $\vec{\xi}$ is relative position vector. As demonstrated by Peerlings et al. [39], Eq. (11) can be approximated by the following differential form:

$$\bar{\varepsilon}_{eq} = \varepsilon_{eq} + l_c^2 \nabla^2 \varepsilon_{eq} \quad (12)$$

where l_c is a material dependent internal length scale parameter representing the dimensions of the micro-structure of the material and ∇^2 represents the Laplacian operator. Apart from the numerical benefits the adoption of a non-local equivalent strain thus reflects the coarse-grained granular material structure represented by the internal length scale l_c . From a numerical point-of-view it is beneficial to transform Eq. (12) into its implicit form [39]:

$$\bar{\varepsilon}_{eq} - l_c^2 \nabla^2 \bar{\varepsilon}_{eq} = \varepsilon_{eq} \quad (13)$$

It has been shown previously [39,42] that the implicit determination of the non-local strain from the applied elliptic partial differential equation gives good results in controlling the predictions of damage models prior to material failure. Eq. (13) reflects that the local equivalent strain can be considered as the source term in the differential equation for the non-local equivalent strain and thus as the governing source for damage evolution.

The evolution of thermal shock damage originates from events at two scales. Long range elastic fields at the macro-scale are induced by the thermal gradients at the continuum level, accounted for in Eq. (13). However, for thermal shock, a second source of damage exists, associated to a fine scale distribution of deformations. This is induced by microscopic temperature gradients acting on the heterogeneous micro-structure where thermal expansion mismatches are present. Hence the temperature gradients may lead to excessive micro-scale stresses and damage. The governing micro-scale deformation is represented by a micro-structural local equivalent strain which is taken to be proportional to the spatial variation of temperature, defined here as

$$\varepsilon_{eq,micro} = r_{ths} |\bar{\theta} - \theta| \quad (14)$$

where r_{ths} is a proportionality constant and the non-local temperature $\bar{\theta}$ is obtained via a weighted average of the local temperature θ within a certain vicinity of the material point concerned, analogically defined as the non-local equivalent strain in Eq. (11). The fine scale influence of temperature gradients on the granular material structure is reflected in Eq. (14). The influence of strain gradients on the micro-scale strains of the heterogeneous materials is thus accounted for. The influence of the local temperature itself is dealt with within the framework of thermal damage. In line with Eq. (12), the non-local temperature $\bar{\theta}$ can be approximated by

$$\bar{\theta} = \theta + l_{ths}^2 \nabla^2 \theta \quad (15)$$

where l_{ths} is a material dependent internal length scale parameter representing the dimensions of the micro-structure of the material and the governing material characteristics which incorporate the previously discussed fine-scale thermo-mechanic behaviour.

Eq. (15) can be substituted into Eq. (14), yielding:

$$\varepsilon_{\text{eq,micro}} = c_{\text{ths}} |\nabla^2 \theta| \quad (16)$$

where the constant c_{ths} replaces the product $r_{\text{ths}} l_{\text{ths}}^2$. Taking into account the diffusion equation for heat transfer without source terms, which reads:

$$\nabla^2 \theta = \frac{1}{\alpha_{\text{dif}}} \dot{\theta} \quad (17)$$

(with the thermal diffusivity $\alpha_{\text{dif}} = \lambda / \rho C_p$, λ the thermal conductivity, ρ the mass density and C_p the heat capacity), it follows that adding the second source term, Eq. (16), to Eq. (13) results in:

$$\bar{\varepsilon}_{\text{eq}} - l_c^2 \nabla^2 \bar{\varepsilon}_{\text{eq}} = \varepsilon_{\text{eq}} + \frac{c_{\text{ths}}}{\alpha_{\text{dif}}} |\dot{\theta}| \quad (18)$$

If temperature changes proceed quasi-stationary the second source term vanishes from Eq. (18). From the definition of α_{dif} it follows from Eq. (18) that a higher thermal conductivity (λ) as well as a lower heat capacity (ρC_p) lead to less thermal shock damage, provided that c_{ths} is not affected.

4. Finite element implementation

This section outlines the implementation of the previously described mathematical model into a Galerkin-based finite element program. The solution process is based on a full Newton–Raphson linearization of the discretized weak forms.

4.1. Weak forms and discretization of the governing equations

The system to be solved consists of the equations for heat transport without internal sources, equilibrium without body forces and the equation for the non-local equivalent strain Eq. (18):

$$\nabla^2 \theta = \frac{1}{\alpha_{\text{dif}}} \dot{\theta} \quad (19)$$

$$\vec{\nabla} \cdot \sigma = \vec{0} \quad (20)$$

$$\bar{\varepsilon}_{\text{eq}} - l_c^2 \nabla^2 \bar{\varepsilon}_{\text{eq}} = \varepsilon_{\text{eq}} + \frac{c_{\text{ths}}}{\alpha_{\text{dif}}} |\dot{\theta}| \quad (21)$$

The boundary conditions involved with the differential equations (19) and (20) are straightforwardly prescribed by the physical problem description. A physically acceptable boundary condition for Eq. (21) reads [39]:

$$\vec{\nabla} \bar{\varepsilon}_{\text{eq}} \cdot \vec{n} = 0 \quad (22)$$

where \vec{n} denotes the normal at the edge of the domain Ω considered. Using a Galerkin discretization of the relevant fields and substitution into the weak forms of Eqs. (19)–(21) yields:

$$\int_{\Omega} \underline{N}_{\theta}^T \rho C_p \underline{N}_{\theta} d\Omega \dot{\theta} + \int_{\Omega} \underline{B}_{\theta}^T \lambda \underline{B}_{\theta} d\Omega \theta = f_{\text{ext}}^{\theta} \quad (23)$$

$$\int_{\Omega} \underline{B}_u^T \sigma d\Omega = f_{\text{ext}}^u \quad (24)$$

$$\int_{\Omega} (\underline{N}_e^T \underline{N}_e \bar{\varepsilon}_{\text{eq}} + \underline{B}_e^T l_c^2 \underline{B}_e \bar{\varepsilon}_{\text{eq}} - \underline{N}_e^T \varepsilon_{\text{eq}}) d\Omega - \int_{\Omega} \underline{N}_e^T \frac{c_{\text{ths}}}{\alpha_{\text{dif}}} \underline{N}_{\theta} d\Omega |\dot{\theta}| = f_{\text{ext}}^e \quad (25)$$

where the matrices \underline{N}_{θ} and \underline{N}_e contain the interpolation functions for temperature and non-local equivalent strain, respectively. The matrices \underline{B}_{θ} , \underline{B}_u and \underline{B}_e contain derivatives of the interpolation functions for temperature, displacement and non-local equivalent strain. The column $\dot{\theta}$ contains the time derivatives of the nodal temperatures. The column σ contains the components of the stress tensor σ . The nodal columns f_{ext}^{θ} , f_{ext}^u and f_{ext}^e represent, respectively, external heat fluxes, external mechanical forces and a column containing external non-local quantities (equaling zero).

4.2. Linearization and incremental-iterative solution procedure

For the temporal discretization of Eqs. (23) and (25) at increment level a Backward–Euler scheme is applied. Linearization of the non-linear system of incremental equations has been performed taking into account the temperature dependency of the thermal conductivity, thermal capacity, Young’s modulus and the ratio of compressive and tensile strength η . Successive

substitution of the linearizations and time discretization into the spatially discretized weak forms Eqs. (23)–(25) yield the following linear system of equations, applicable for iteration step i :

$$\underline{K}_{i-1} \delta \tilde{\mathbf{a}} = \tilde{f}_{\text{ext}} - \tilde{f}_{\text{int},i-1} \quad (26)$$

with \underline{K}_{i-1} the system matrix, $\delta \tilde{\mathbf{a}}$ the column with adaptations of the estimated values of the nodal temperatures, the nodal displacements and the nodal non-local equivalent strains and $\tilde{f}_{\text{int},i-1}$ the column with nodal reactions. In a decomposed format the iteration equation (27) can be written as

$$\underline{K}_{i-1} = \begin{bmatrix} \underline{K}_{i-1}^{\theta\theta} & \underline{K}_{i-1}^{\theta u} & \underline{K}_{i-1}^{\theta e} \\ \underline{K}_{i-1}^{u\theta} & \underline{K}_{i-1}^{uu} & \underline{K}_{i-1}^{ue} \\ \underline{K}_{i-1}^{e\theta} & \underline{K}_{i-1}^{eu} & \underline{K}_{i-1}^{ee} \end{bmatrix}, \quad \delta \tilde{\mathbf{a}} = \begin{bmatrix} \delta \tilde{\theta} \\ \delta \tilde{\mathbf{u}} \\ \delta \tilde{\boldsymbol{\varepsilon}}_{\text{eq}} \end{bmatrix}, \quad \tilde{f}_{\text{ext}} = \begin{bmatrix} \tilde{f}_{\text{ext}}^{\theta} \\ \tilde{f}_{\text{ext}}^u \\ \tilde{f}_{\text{ext}}^e \end{bmatrix}, \quad \tilde{f}_{\text{int},i-1} = \begin{bmatrix} \tilde{f}_{\text{int},i-1}^{\theta} \\ \tilde{f}_{\text{int},i-1}^u \\ \tilde{f}_{\text{int},i-1}^e \end{bmatrix} \quad (27)$$

In Eq. (27) the sub-matrices $\underline{K}_{i-1}^{\theta u}$ and $\underline{K}_{i-1}^{\theta e}$ consist entirely of zero elements indicating that the temperature field is not influenced by damage development i.e. it is assumed that the thermal moduli do not depend on damage. For a more detailed elaboration of the remaining sub-matrices and sub-columns in Eq. (27) reference is made to the Appendix.

4.3. Computational solution issues

The sub-matrices composing the global system matrix (Eq. (27)) are determined at the element level. Within the three-dimensional element, the temperature and non-local equivalent strain are approximated using tri-linear interpolation functions. The displacement components are approximated using quadratic interpolation functions in a serendipity configuration. Using the same order of interpolation might lead to stress oscillations as was found by Peerlings [42]. Within the context of the proposed quadratic displacement discretization the local elastic strain becomes of reduced order in agreement with the lower order damage stemming from the lower order temperature and non-local equivalent strain. It has been found that this approach gives good results when combined with reduced Gauss integration of the equilibrium equation and full integration of the field equation for the non-local equivalent strain, Eq. (21) [42]. Full Gauss integration has been applied for the heat transport equation as well. Note that this implies that eight integration points are used to evaluate the contributions for thermal diffusion, equilibrium and the non-local equivalent strain. Eventually this leads to a 20-noded quadratic serendipity finite element where the displacement components are evaluated at all nodes and the temperature and non-local equivalent strain only at the corner nodes.

5. Non-local aspects of thermal shock damage

The influence of the contribution of the transient temperature gradients in the non-locality equation (Eq. (21)) as well as the effect of an increasing internal length scale are investigated in sensitivity analyses. The influence of the value assigned to the thermal shock constant c_{ths} and to the intrinsic length l_c (Eq. (18)) has been investigated by the analysis of five cases (A–E), summarized in Table 1. Fig. 2 shows the geometry and boundary conditions used in the analysis which is performed in a plane strain context. The homogeneous initial sample temperature θ_0 equals 20 °C. The bottom sample side is subject to a temperature jump of 1500 °C. Symmetry conditions apply to the left sample side. The vertical displacements are constrained on the upper sample side, which is also thermally insulated. The right sample side is thermally insulated. Eqs. (28) and (29) specify the temperature-dependent thermal capacity and conductivity, based on measurements on typical refractory material in the relevant temperature regime

$$C_p(\theta) = 782 + 0.3\theta + 0.0003\theta^2 \quad [\text{J/kg K}] \quad (28)$$

$$\lambda(\theta) = 1.979 + 0.0008\theta + 6 \times 10^{-7}\theta^2 \quad [\text{W/m K}] \quad (29)$$

where θ is expressed in °C. The values of the model parameters used in this analysis are typical for refractory material. The density, Young's modulus, Poisson's ratio and thermal expansion coefficient used are, respectively, 2220 kg/m³, 15 GPa, 0.2 and 6×10^{-6} K⁻¹. For the parameter η in the modified Von Mises definition, Eq. (9), a value of 4 has been selected. For the parameters α , β and $\kappa_{\text{el},i}$ in Eq. (5) respective values of -1, 10 and 8×10^{-4} have been chosen. Thermal damage was not activated. A discretization of 20×40 square elements has been used. A time frame of 30 s was analyzed using time steps of 0.5 s.

Table 1
Values of thermal shock constant and internal length scale used in the parameter sensitivity analysis

	Case number				
	A	B	C	D	E
c_{ths} (m ² /K)	0	2.5×10^{-12}	5.0×10^{-12}	0	0
l_c (mm)	3	3	3	1	5

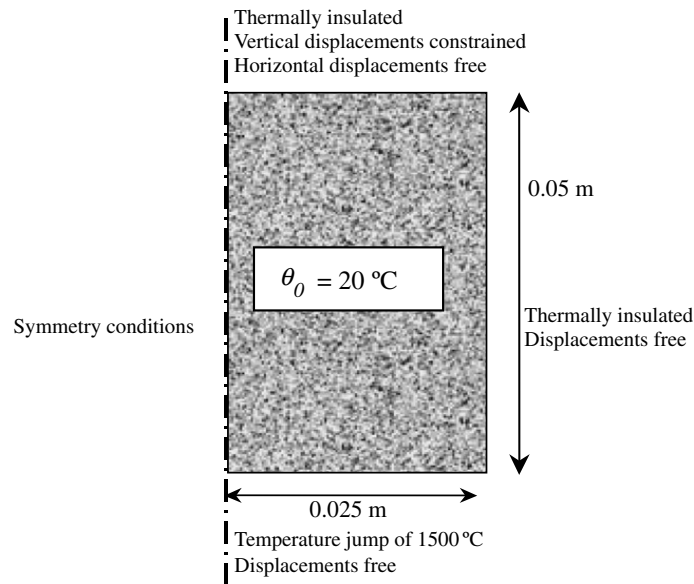


Fig. 2. Sample subject to an upquench thermal shock.

Fig. 3 shows the results for case C at 10 s. Compared to the local equivalent strain the non-local equivalent strain is more smooth and has a lower maximum value. This is due to the averaging effect of the non-local formulation on the local equivalent strain field. The high values of the damage at the sample bottom are due to the thermal shock term in Eq. (18). This can also be observed in Fig. 4 which depicts the centerline non-local equivalent strain and damage as a function of time for the cases A–C. With increasing values of the thermal shock constant c_{ths} the damage at the sample bottom increases while the damage at quarter height and half height decreases slightly. The decrease in damage is due to the aforementioned averaging effect of non-locality. The time at which the maximum in damage is reached (event time), for quarter and half sample heights, hardly changes for the considered values of the thermal shock constant.

Fig. 5 shows the additional time-dependent results for the non-local equivalent strain and the damage, for cases D and E. The influence of an increased value of the internal length scale can be investigated by comparing cases D, A and E. It can be observed that with increasing internal length scale the damage decreases. This applies especially at quarter height and half height and considerably less at the quenched sample side. The aforementioned event time is roughly the same for all cases D, A and E. Most damage does not appear at the sample bottom but at higher locations in the sample, which is due to the stress distribution. At the sample bottom compressive stresses prevail due to restricted thermal expansion (due to less expansion at higher locations). Reversely, at higher locations tensile stresses can be found. The definition for the local equivalent strain, Eq. (9), entails a higher (elasticity-based) damage evolution in case of tensile loading. For the maximum applied internal length scale (case E) the averaging effect of non-locality is such that even at the bottom of the sample, damage growth nearly stops after 10 s just as for the higher locations.

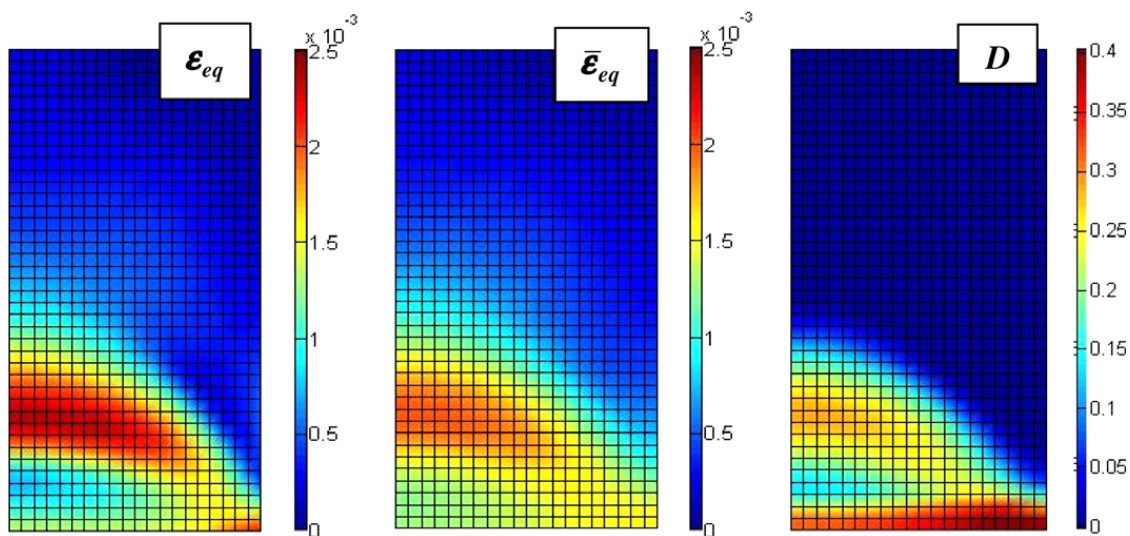


Fig. 3. Results for case C ($c_{\text{ths}} = 5 \times 10^{-12} \text{ m}^2/\text{K}$, $l_c = 3 \text{ mm}$) at $t = 10 \text{ s}$.

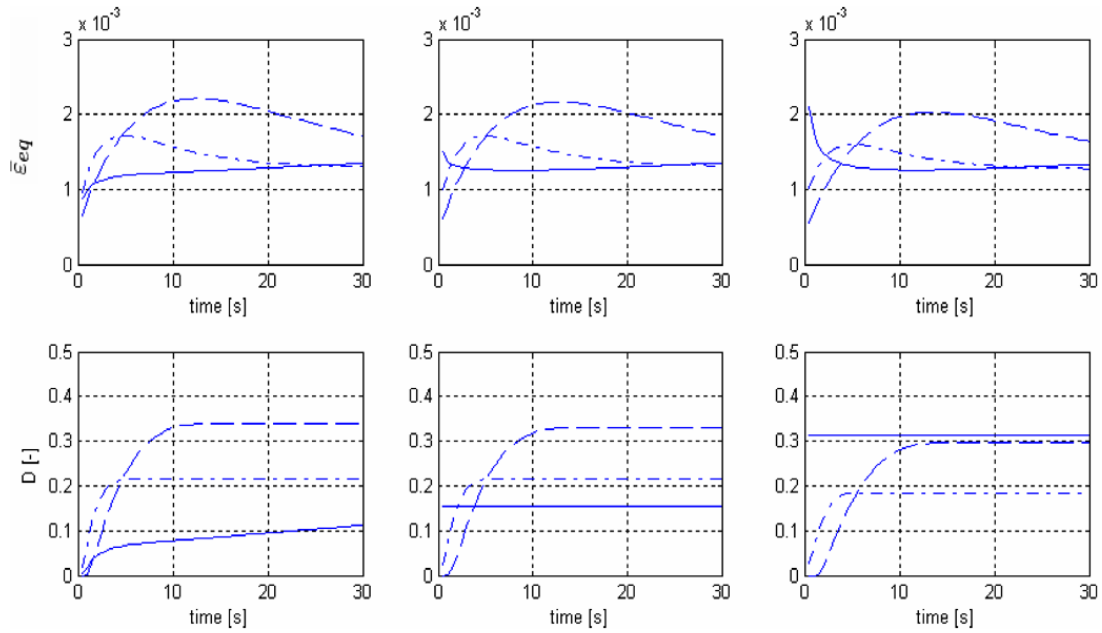


Fig. 4. Centerline non-local equivalent strain (upper row) and damage (lower row) as a function of time for the cases A–C (left to right). Solid line: sample bottom, dash-dot: quarter height, dashed: half height.

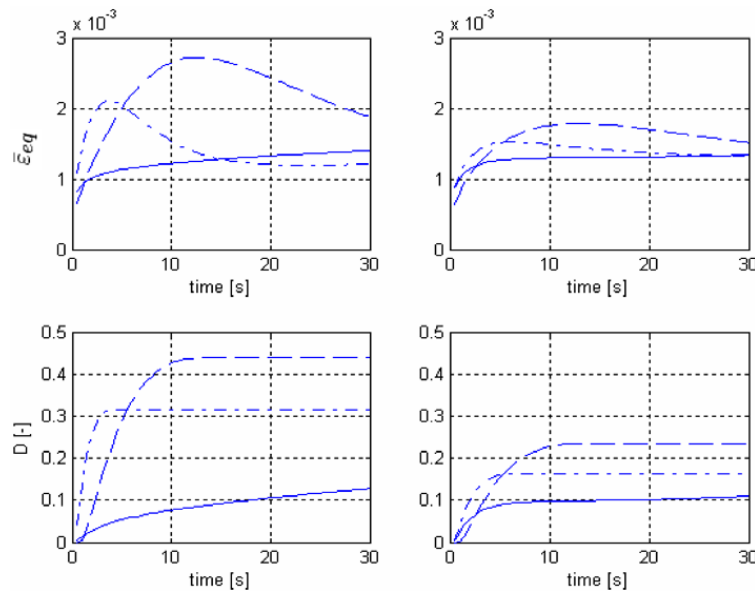


Fig. 5. Centerline non-local equivalent strain (upper row) and damage (lower row) as a function of time for the cases D and E (left to right). Solid line: sample bottom, dash-dot: quarter height, dashed: half height.

6. Thermal shock experiments

The numerical model was used to simulate dedicated thermal shock experiments where refractory samples of ambient temperature were quenched in molten aluminium of 1000 °C. Damage in the samples was determined from sound measurements. Calculated damage is compared with experimental damage.

6.1. Set-up and experimental procedures

The left part of Fig. 6 shows a schematic view of the set-up and samples used. Solid aluminium was molten and heated to 1000 °C in an open induction furnace, powerful enough to maintain the temperature at a constant level. On top of the furnace a guiding system was mounted which enabled accurate and fast positioning of a sample in contact with the liquid aluminium bath. The sample is connected to the guiding system by a ceramic rod of low thermal conductivity. The sample temperature

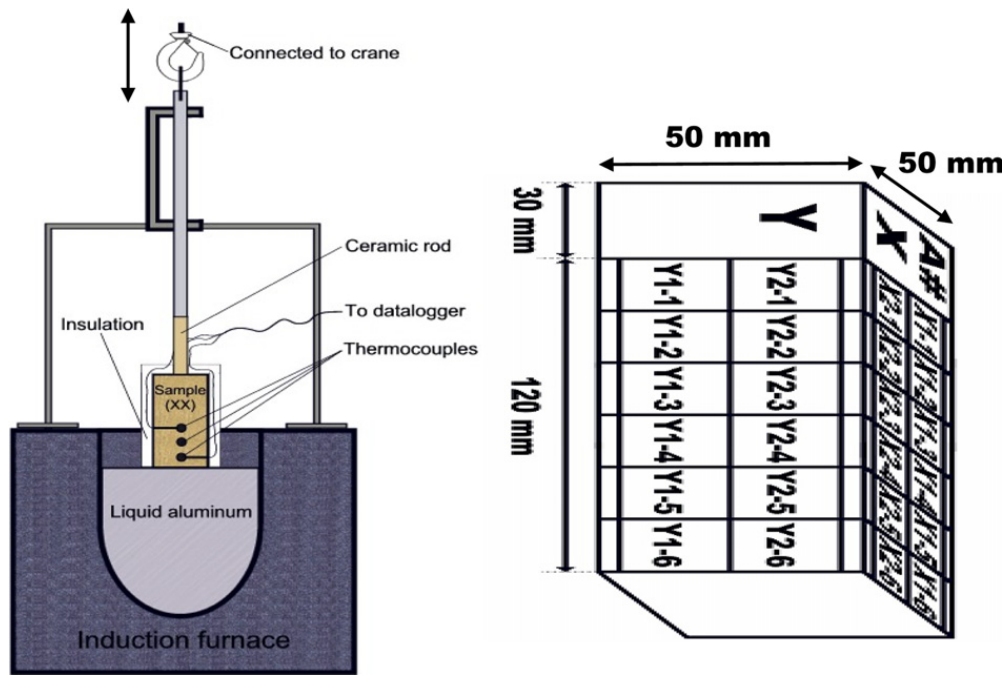


Fig. 6. Schematic view of the set-up used in the thermal shock experiments (left) and sample with measurement grid, not to scale (right).

was measured with thermocouples located on its centerline at 10, 25 and 40 mm from the sample bottom. Samples without thermocouples were used for damage determination. Apart from the quenched side all other sides were thermally insulated. Terracoat® was applied at the quenched side to prevent aluminium penetration into the sample. The heating period was 20 min after which the sample was exposed to ambient air.

The sound velocity in the sample was determined before and after the experiment. The right part of Fig. 6 shows the measurement grid used. Transducers were positioned opposite to each other at four different locations, e.g., at Y1-1, Y2-1, X2-1 and X1-1 for six positions on the longitudinal sample axis. For each position along the longitudinal axis results were averaged over these four locations. From the measured transit time of longitudinal sound waves and the mutual transducer distance the average sound velocity was calculated. Subsequently, the dynamic Young's modulus E was calculated using Eq. (30) where V and ν specify the sound velocity and Poisson's ratio, respectively. Damage causes an increase in transit time and thus a decrease in sound velocity and dynamic Young's modulus. The relative change of the latter is used to calculate the damage from Eq. (31), assuming that the sample density and Poisson's ratio are not affected by the damage:

$$E = \rho \left[\frac{(1 + \nu)(1 - 2\nu)}{(1 - \nu)} \right] V^2 \quad (30)$$

$$D = \frac{E_0 - E}{E_0} \quad (31)$$

6.2. Results of the experiments and modeling

Fig. 7 shows the experimentally determined damage obtained for three samples (denoted by A1, A2 and A3) and modeling results, to be discussed in the following. The damage measured is most severe near the quenched sample sides where temperature gradients are the highest.

The thermal shock experiments were modeled with appropriate symmetry conditions for only a quarter of the sample (with dimensions: width \times depth \times height of $25 \times 25 \times 150 \text{ mm}^3$). The vertical displacement of the top centerline node is constrained consistent with the sample mounting. At the quenched sample side a temperature of $1000 \text{ }^\circ\text{C}$ is prescribed. The other sample sides are modeled as insulated. The heating period of 20 min was modeled using time steps of 3 s. The cooling period was not considered due to the relatively low heat transfer coefficient, which has been determined from the measured temperatures by inverse heat transfer modeling. A mesh density of $6 \times 6 \times 36$ (width \times depth \times height) brick elements was used. The parameters identifying the material behaviour are presented in Table 2. Some parameters are based on standard measurements in the temperature zone of interest, which are given as functions of the temperature θ expressed in $^\circ\text{C}$. The Young's modulus and the damage threshold value for elasticity-based damage were determined from three-point bending tests. The coefficient of thermal expansion was determined from dilatation measurements. The thermal conductivity and capacity were determined with standard measurements. The ratio of compressive and tensile strength (parameter η in Eq. (9)) was determined from uni-axial compressive tests and three-point bending tests for different temperature levels.

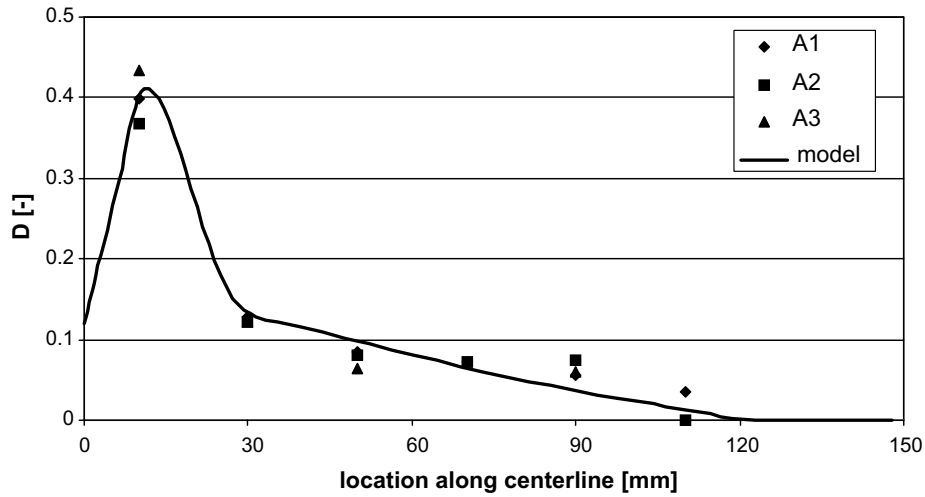


Fig. 7. Comparison between experimental and calculated damage.

Table 2

Parameters used in the modeling of the thermal shock experiments

Type	Quantity	Value	Unit	Source
Elastic material parameters	Young's modulus	$E(\theta) = -0.0971\theta^4 + 86.188\theta^3 + 4929.1\theta^2 - 1 \times 10^{-6}\theta + 1 \times 10^{10}$	Pa	Measured
	Poisson's ratio	$\nu = 0.22$	[-]	Estimate
Thermo-elastic material parameters	Thermal expansion	$\alpha_{th} = 5.8 \times 10^{-6}$	K^{-1}	Measured
Thermal material parameters	Density	$\rho = 2220$	kg/m^3	
	Conductivity	$\lambda(\theta) = 1.979 + 0.0008\theta + 6 \times 10^{-7}\theta^2$	$W/m K$	
Equivalent strain parameter	Capacity	$C_p(\theta) = 782 + 0.3\theta + 0.0003\theta^2$	$J/kg K$	
	Compression/tension strength	$\eta(\theta) = 3 \times 10^{-6}\theta^2 - 0.0001\theta + 2.9973$	[-]	
Non-local material parameters	Length scale	$l_c = 3$	mm	Estimate
	Thermal shock constant	$c_{ths} = 5 \times 10^{-12}$	m^2/K	Fitting result
Elasticity-based damage parameters	Damage threshold value	$\kappa_{el,i}(\theta) = 0.0008 - 8 \times 10^{-8}\theta + 10^{-10}\theta^2$	[-]	Measured
	Damage evolution parameters	$\alpha = -1.25$	[-]	Fitting result
		$\beta = 1250$	[-]	Fitting result
Thermal damage parameters	Damage threshold value	$\kappa_{th,i} = 50$	$^{\circ}C$	
	Damage evolution parameters	$\phi = 0.3184$	[-]	
		$\kappa_{th,c} = 19,000$	$^{\circ}C$	

The value of Poisson's ratio used, 0.22, was estimated from typical values for refractory materials. Given the average material grain size of about 3 mm a value of the internal length scale parameter l_c equal to 3 mm was used. To ensure that the calculated damage at the sample bottom agreed with the trend in the corresponding experimental damage, a value of the thermal shock constant c_{ths} of $5 \times 10^{-12} m^2/K$ was used. The damage parameters (α , β , $\kappa_{th,i}$, ϕ , $\kappa_{th,c}$) are estimated by fitting the numerical and experimental results.

Fig. 8 shows the evolution of the centerline temperature rate and non-local equivalent strain. Fig. 9 shows the evolution of the centerline temperature and total damage. Fig. 8 illustrates that, compared to the maximum values of the temperature rate, the maximum values of the corresponding non-local equivalent strain are shifted to a somewhat higher location in the sample. The evolution of the temperature rate and non-local equivalent strain indicate that the elasticity-based damage is concentrated in the lowest two centimeters of the sample. This is confirmed by the comparison of the evolution of the (maximum) temperature (the driving variable for thermal damage) and the damage (Fig. 9). At higher positions in the sample only thermal damage is present. Its evolution stops when the sample temperature reaches 50 °C after 20 min, at 0.12 m.

Fig. 7 demonstrates that experiments and calculations compare well; also experimental results point towards the presence of elasticity-based damage in the lowest two centimeters of the sample. The parameters α and β used are normally temperature-independent. For refractory materials, however, these parameters are likely to be temperature-dependent as they affect the post-elastic temperature-dependent stress–strain behaviour, see e.g. Fig. 1 and Eq. (3). This implies that the parameter values identified here should be regarded as a first attempt to establish the phenomenological relevance of the model. Their uniqueness cannot be proven. The temperature-dependent nature of α and β can be determined from e.g. uni-axial

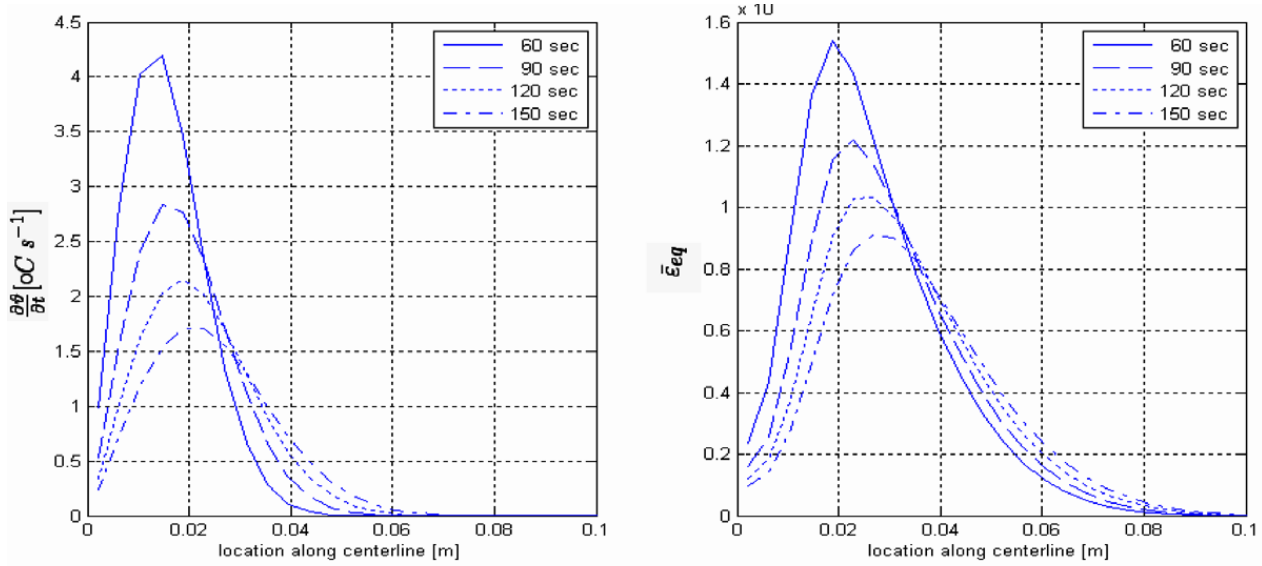


Fig. 8. Temperature rate (left) and non-local equivalent strain (right) along the centerline.

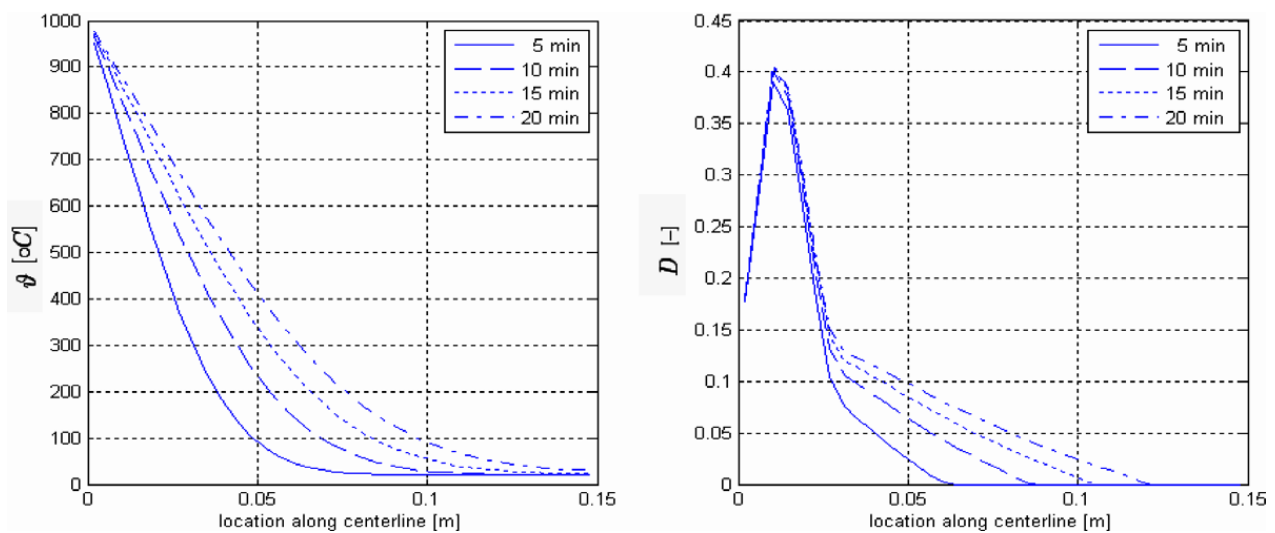


Fig. 9. Temperature (left) and damage (right) along the centerline.

compression and bending tests performed at the temperatures of interest [33,34,37,38]. The parameters governing the thermal damage evolution can be obtained from furnace experiments where samples are heated quasi-stationary to ensure a spatially uniform temperature. The difference between the measured initial and residual properties determines the thermal damage, which can be used to, e.g., calculate the parameters in Eq. (7). The intrinsic length scale parameter l_c and thermal shock constant c_{ths} are a.o. dependent on the dimensions of the micro-structure. If the parameters of the damage evolution laws are known, l_c and c_{ths} can be determined from dedicated experiments reflecting this size-dependent nature of damage [43].

7. Conclusions

The principal causes of premature failure of refractory materials in installations for iron- and steel-making are fatal thermal stresses induced by high transient temperature gradients, a phenomenon also known as thermal shock. In coarse-grained refractory material this initially leads to diffuse micro-cracking and can be followed by localization to macro-cracks pending on the load severity.

To capture the post-elastic transient thermo-mechanical behaviour of refractory materials a modeling framework has been developed based on continuum damage mechanics. To describe thermal shock damage a single scalar variable is used

affecting the temperature-dependent Young's modulus with contributions from two distinct damage mechanisms. The first damage mechanism (elasticity-based damage) is induced by elastic strains stemming from temperature gradients causing internally and externally constrained thermal expansion. The second damage mechanism (thermal damage) is driven by uniform temperature change. This causes isotropic thermal expansion which can induce damage (e.g. micro-cracks) in case thermal expansion mismatches exist between the various constituents (e.g. grains, matrix). This structural phenomenon might be amplified by, e.g., phase transitions in certain material components resulting in a permanent degradation of Young's modulus.

Compared to previous work the modeling framework presented in this paper comprises the following new aspects:

- The elasticity-based and thermal damage are combined in an additive way, driven by the assumption that both damage mechanism act independently on different scales.
- The driving variable for elasticity-based damage, the non-local equivalent strain, obtained via a gradient enhanced implicit formulation, is extended with a term accounting for micro-structural strain gradients induced by transient temperature gradients.
- Within the definition used for the local equivalent strain (modified Von Mises) a temperature-dependent ratio of compressive and tensile strength is incorporated. Other parameters in the framework proposed for elasticity-based damage also reflect the distinct temperature-dependent mechanical behaviour of refractory material.
- For thermal damage a new evolution law is proposed enabling progressive as well as degressive evolution with the attained maximum temperature.
- The equations for transient thermal transport, equilibrium and extended (transient) non-locality and are solved simultaneously in a finite element environment using a Backward-Euler time integration scheme and full Newton–Raphson linearization. Temperature-dependent elastic and thermal moduli are used where appropriate. The transient evolution of non-local damage combined with temperature-dependent parameters has not been described before elsewhere.

The influence of non-locality and its (micro-structural strain gradient) extension has been investigated in a parameter study within a plane strain context. Due to the averaging effect of a non-local formulation, damage decreased and became less localized for an increasing internal length scale (reflecting the coarseness of refractory material). This did not influence the time at which the maximum equivalent strain, the source term for the actual elasticity-based damage, reached maximum values. Increase in the micro-structural strain gradient contribution was apparent through extra damage at the thermally shocked edge, despite the compressive stress state at that location.

The phenomenological relevance of the numerical framework was established through a model of a dedicated thermal shock experiment where ambient refractory samples have been brought in contact with molten aluminium. The temperature-dependent thermal and elastic material properties used were obtained from standard measurements. The values of the parameters governing the evolution of elasticity-based and thermal damage were identified from the obtained experimental results showing an adequate agreement. Elasticity-based damage was present in the immediate vicinity of the quenched sample side while in the remainder of the material thermal damage could be observed. Differences between model and experiments might be reduced by using temperature-dependent damage evolution parameters reflecting the temperature-dependent (post-elastic) constitutive behaviour. The determination of such parameters with dedicated tests will be part of future work.

Appendix

The linear system of equations to be solved within the numerical modeling framework presented in this paper (Eq. (28)) reads:

$$\underline{K}_{i-1} \delta \tilde{a} = \tilde{f}_{\text{ext}} - \tilde{f}_{\text{int},i-1} \quad (\text{A1})$$

with the following components

$$\underline{K}_{i-1} = \begin{bmatrix} \underline{K}_{i-1}^{\theta\theta} & \underline{K}_{i-1}^{\theta u} & \underline{K}_{i-1}^{\theta e} \\ \underline{K}_{i-1}^{u\theta} & \underline{K}_{i-1}^{uu} & \underline{K}_{i-1}^{ue} \\ \underline{K}_{i-1}^{e\theta} & \underline{K}_{i-1}^{eu} & \underline{K}_{i-1}^{ee} \end{bmatrix}, \quad \delta \tilde{a} = \begin{bmatrix} \delta \tilde{\theta} \\ \delta \tilde{u} \\ \delta \tilde{\varepsilon}_{\text{eq}} \end{bmatrix}, \quad \tilde{f}_{\text{ext}} = \begin{bmatrix} \tilde{f}_{\text{ext}}^{\theta} \\ \tilde{f}_{\text{ext}}^u \\ \tilde{f}_{\text{ext}}^e \end{bmatrix}, \quad \tilde{f}_{\text{int},i-1} = \begin{bmatrix} \tilde{f}_{\text{int},i-1}^{\theta} \\ \tilde{f}_{\text{int},i-1}^u \\ \tilde{f}_{\text{int},i-1}^e \end{bmatrix} \quad (\text{A2})$$

The sub-matrices of the global system matrix \underline{K}_{i-1} are presented below in row-wise order.

Row 1

$$\underline{K}_{i-1}^{\theta\theta} = \underline{L}_{1,i-1} + \underline{L}_{2,i-1} + \underline{L}_{3,i-1} + \underline{L}_{4,i-1} \quad (\text{A3})$$

where the abbreviations $\underline{L}_{1,i-1}$, $\underline{L}_{2,i-1}$, $\underline{L}_{3,i-1}$ and $\underline{L}_{4,i-1}$ denote

$$\begin{aligned}
 \underline{L}_{1,i-1} &= \int_{\Omega} \underline{N}_{\theta}^T \rho \left(\frac{\partial C_p}{\partial \theta} \right)_{i-1} \left(\underline{N}_{\theta} \frac{\theta_{i-1} - \theta_n}{\Delta t} \right) \underline{N}_{\theta} d\Omega \\
 \underline{L}_{2,i-1} &= \int_{\Omega} \underline{N}_{\theta}^T \rho C_{p,i-1} \underline{N}_{\theta} d\Omega \frac{1}{\Delta t} \\
 \underline{L}_{3,i-1} &= \int_{\Omega} \underline{B}_{\theta}^T \left(\frac{\partial \lambda}{\partial \theta} \right)_{i-1} \underline{B}_{\theta} \theta_{i-1} \underline{N}_{\theta} d\Omega \\
 \underline{L}_{4,i-1} &= \int_{\Omega} \underline{B}_{\theta}^T \lambda_{i-1} \underline{B}_{\theta} d\Omega \\
 \underline{K}_{i-1}^{uu} &= \underline{K}_{i-1}^{\theta e} = \underline{0}
 \end{aligned} \tag{A4}$$

Row 2

$$\underline{K}_{i-1}^{u\theta} = \underline{S}_{1,i-1} + \underline{S}_{2,i-1} + \underline{S}_{3,i-1} \tag{A5}$$

where the abbreviations $\underline{S}_{1,i-1}$, $\underline{S}_{2,i-1}$ and $\underline{S}_{3,i-1}$ denote

$$\begin{aligned}
 \underline{S}_{1,i-1} &= - \int_{\Omega} \underline{B}_u^T [R(d_{el}, \kappa_{el}, \bar{\varepsilon}_{eq}) + R(d_{el}, \kappa_{el,i}, \theta) + R(d_{el}, \alpha, \theta) + \dots + R(d_{el}, \beta, \theta) + R(d_{th}, \kappa_{th}, \theta)] \underline{C}_{i-1} \varepsilon_{el,i-1} d\Omega \\
 \underline{S}_{2,i-1} &= \int_{\Omega} \underline{B}_u^T (1 - d_{el,i-1} - d_{th,i-1}) \left(\frac{\partial \underline{C}}{\partial E} \right)_{i-1} \left(\frac{\partial E}{\partial \theta} \right)_{i-1} \varepsilon_{el,i-1} \underline{N}_{\theta} d\Omega \\
 \underline{S}_{3,i-1} &= - \int_{\Omega} \underline{B}_u^T (1 - d_{th,i-1} - d_{th,i-1}) \underline{C}_{i-1} \underline{N}_{\theta} d\Omega
 \end{aligned}$$

In the expression for $\underline{S}_{1,i-1}$, in the above, the abbreviation $R(F,G,H)$ has been used for clarity such that, e.g.,

$$\begin{aligned}
 R(F, G, H) &= \left(\frac{\partial F}{\partial G} \right)_{i-1} \left(\frac{\partial G}{\partial H} \right)_{i-1} \underline{N}_H \\
 \underline{K}_{i-1}^{uu} &= \int_{\Omega} \underline{B}_u^T (1 - d_{th,i-1} - d_{el,i-1}) \underline{C}_{i-1} \underline{B}_u d\Omega
 \end{aligned} \tag{A6}$$

$$\underline{K}_{i-1}^{ue} = - \int_{\Omega} \underline{B}_u^T \left(\frac{\partial d_{el}}{\partial \kappa_{el}} \right)_{i-1} \left(\frac{\partial \kappa_{el}}{\partial \bar{\varepsilon}_{eq}} \right)_{i-1} \underline{C}_{i-1} \varepsilon_{el,i-1} \underline{N}_e d\Omega \tag{A7}$$

Row 3

$$\underline{K}_{i-1}^{e\theta} = \int_{\Omega} \underline{N}_e^T \left(\left(\frac{\partial \varepsilon_{eq}}{\partial \varepsilon_{el}} \right)_{i-1}^T m - \left(\frac{\partial \varepsilon_{eq}}{\partial \eta} \right)_{i-1} \left(\frac{\partial \eta}{\partial \theta} \right)_{i-1} - \left(\frac{\partial C_{ths}}{\partial \theta} \right)_{i-1} \underline{N}_{\theta} \left| \frac{\theta_{i-1} - \theta_n}{\Delta t} \right| \right) \underline{N}_{\theta} d\Omega \tag{A8}$$

$$\underline{K}_{i-1}^{eu} = - \int_{\Omega} \underline{N}_e^T \left(\frac{\partial \varepsilon_{eq}}{\partial \varepsilon_{el}} \right)_{i-1}^T \underline{B}_u d\Omega \tag{A9}$$

$$\underline{K}_{i-1}^{ee} = \int_{\Omega} (\underline{N}_e^T \underline{N}_e + \underline{B}_e^T l_c^2 \underline{B}_e) d\Omega \tag{A10}$$

References

- [1] Hasselman DPH. Thermal stress resistance parameters for brittle refractory ceramics: a compendium. *Ceram Bull* 1970;49:1033–7.
- [2] Hasselman DPH. Figures-of-merit for the thermal stress resistance of high-temperature brittle materials: a review. *Ceram Int* 1978;4:147–50.
- [3] Hasselman DPH. Unified theory of thermal shock fracture initiation and crack propagation in brittle ceramics. *J Am Ceram Soc* 1969;52:600–4.
- [4] Lu TJ, Fleck NA. The thermal shock resistance of solids. *Acta Metall Mater* 1998;46:4744–68.
- [5] Bahr HA, Balke H, Kuna M, Lieske H. Fracture analysis of a single edged cracked strip under thermal shock. *Theor Appl Fract Mech* 1987;8:33–9.
- [6] Bahr HA, Fett T, Hahn I, Munz D, Pflugbeil I. Fracture mechanics treatment of thermal shock and the effect of bridging stresses. Thermal shock and thermal fatigue behaviour of advanced ceramics. Kluwer Academic Publishers; 1993. p. 105–117.
- [7] Wu XR. Application of weight function method for crack analysis in thermal stress fields. Thermal shock and thermal fatigue behaviour of advanced ceramics. Kluwer Academic Publishers; 1993. p. 119–141.
- [8] Cotterel B, Sze WO, Caidong Q. Thermal shock and size effects in castable refractories. *J Am Ceram Soc* 1995;78:2056–64.
- [9] Jin ZH, Mai YW. Effects of damage on thermal shock strength behavior of ceramics. *J Am Ceram Soc* 1995;78:1873–81.
- [10] Jin ZH, Batra RC. Thermal shock cracking in a metal-particle-reinforced ceramic matrix composite. *Engng Fract Mech* 1999;62:339–50.
- [11] Soboyejo WO, Mercer C. Investigation of thermal shock in a high-temperature refractory ceramic: a fracture mechanics approach. *J Am Ceram Soc* 2001;84:1309–14.
- [12] Rubesa D. Thermal stress fracture and spalling of well blocks in steel ladles – modeling and numerical simulation. *Veitsch-Radex Rundschau* 1999;2:3–24.
- [13] Bradley F, Chaklader ACD, Mitchell A. Thermal stress fracture of refractory lining components. Part 1: Thermo-elastic analysis. *Metall Trans* 1987;18B:355–63.
- [14] Knauder J, Rathner R. Thermo-mechanical analysis of basic refractories. *Radex-Rundschau* 1990;4.

- [15] Schneider JP, Coste B. Thermo-mechanical modeling of thermal shock in anodes. In: Proceedings of the conference on light metals. The Minerals, Metals & Materials Society; 1993.
- [16] Keisuke A. Evaluation of thermal stress in refractory bricks by the finite element method. *Taikabutsu Overseas* 1989;10(4).
- [17] Knauder J, Rathner R. Improved design of a BOF-lining based on thermo-mechanical analysis. *Radex-Rundschau* 1990;1.
- [18] Rathner R. Lining design and behavior of BOF's. *Radex-Rundschau* 1990;4.
- [19] Andreev K, Harmuth H. Application of finite element modeling to the thermo-mechanical behaviour of refractories. In: Hendriks, Rots, editors. Finite elements in civil engineering applications. Swets & Zeitlinger; 2002.
- [20] Andreev K, Harmuth H. FEM simulation of the thermo-mechanical behavior and failure of refractories – a case study. *J Mater Process Technol* 2003; 143–144:72–7.
- [21] van Gils MAJ, Dortmans LJM, de With G. Thermal shock predictions for refractory ceramics. In: Hetnarski RB, Noda N, Ghoneim H, editors. Proceedings of the second international symposium on thermal stresses and related topics. Rochester Institute of Technology; 1997. p. 682–97.
- [22] Schmitt N, Burr A, Berthaud Y, Poirier J. Micro mechanics applied to the thermal shock behavior of refractory ceramics. *Mech Mater* 2002;34:725–47.
- [23] Gasser A, Terry-Rebeyrotte K, Boisse P, Poirier J. A multi-scale approach for refractory structure modeling. In: Smith JD, editor. Proceedings of the unified international technical conference on refractories. The American Ceramic Society; 2005. p. 998–1002.
- [24] Simonin F, Olagnon C, Maximilien S, Fantozzi G, Diaz LA, Torrecillas R. Thermo-mechanical behaviour of high-alumina refractory castables with synthetic spinel additions. *J Am Ceram Soc* 2000;83:2481–90.
- [25] Aksel C, Rand B, Riley FL, Warren PD. Thermal shock behaviour of magnesia-spinel composites. *J Eur Ceram Soc* 2004;24:2839–45.
- [26] Aksel C, Warren PD, Riley FL. Fracture behaviour of magnesia and magnesia-spinel composites before and after thermal shock. *J Eur Ceram Soc* 2004;24:2407–16.
- [27] Bousuge M. Some numerical approaches of creep, thermal shock, damage and delayed failure of ceramics and refractories. *Bull Mater Sci* 2001;24:97–100.
- [28] Bousuge M. Thermo-mechanical behaviour: from ceramics to refractories. Advances in refractories for the metallurgical industries IV. In: Rigaud M, Allaire C, editors. Proceedings of the 43rd annual conference of metallurgists of CIM; 2004.
- [29] Chaboche JL. Continuum damage mechanics. Part I: General concepts. *J Appl Mech* 1988;55:59–64.
- [30] Headrick WL, Karukus M, Laing X. Refractory for black liquor gassifiers. University of Missouri-Rolla, Rolla, MO 65409-1130, DOE Award Number DE-FC26-02NT41491; 2005.
- [31] Prompt N, Ouedraogo E, Joly T, Stutz P. Thermo-mechanical modeling of a refractory structure: the wear layer of a blast furnace trough. In: Proceedings of the unified international technical conference on refractories. The American Ceramic Society; 2001. p. 282–8.
- [32] Liang X, Headrick WL, Dharani LR, Zhao S, Wei J. Failure analysis of refractory cup under thermal loading and chemical attack using continuum damage mechanics. In: Smith JD, editor. Proceedings of the unified international technical conference on refractories. The American Ceramic Society; 2005. p. 980–4.
- [33] Nentech W, Meftah F, Reynouard JM. An elasto-plastic damage model for plain concrete subjected to high temperatures. *Engng Struct* 2002;24:597–611.
- [34] Luccioni BM, Figueroa MI, Danesi RF. Thermo-mechanic model for concrete exposed to elevated temperatures. *Engng Struct* 2003;25:729–42.
- [35] Gawin D, Majorana CE, Schrefler BA. Numerical analysis of hygro-thermal behaviour and damage of concrete at high temperature. *Mech Cohes Frict Mater* 1999;4:37–44.
- [36] Stabler J, Baker G. On the form of free energy and specific heat in coupled thermo-elasticity with isotropic damage. *Int J Solid Struct* 2000;37:4691–713.
- [37] Stabler J, Baker G. Fractional step methods for thermo-mechanical damage analyses at transient elevated temperatures. *Int J Numer Method Engng* 2000;48:761–85.
- [38] Pearce CJ, Nielsen CV, Bicanic N. Gradient-enhanced thermo-mechanical damage for concrete at high temperatures including transient thermal creep. *Int J Numer Anal Method Geomech* 2004;28:715–35.
- [39] Peerlings RHJ, de Borst R, Brekelmans WAM, de Vree JHP. Gradient enhanced damage for quasi-brittle materials. *Int J Numer Method Engng* 1996;39:3391–403.
- [40] Peerlings RHJ, de Borst R, Brekelmans WAM, Geers MGD. Gradient-enhanced damage modeling of concrete fracture. *Mech Cohes Frict Mater* 1998;3:321–42.
- [41] Aksel C. Mechanical properties and thermal shock behaviour of alumina-mullite-zirconia and alumina-mullite refractory materials by slip casting. *Ceram Int* 2003;29:311–6.
- [42] Peerlings RHJ. Enhanced damage modeling for fracture and fatigue. PhD thesis, Technical University of Eindhoven; 1999.
- [43] Geers MGD, de Borst R, Brekelmans WAM, Peerlings RHJ. Strain-based transient-gradient damage model for failure analyses. *Comput Method Appl Mech Engng* 1998;160:133–53.